New total electron content retrieval improves SMOS sea surface salinity

Jean-Luc Vergely, Philippe Waldteufel, Jacqueline Boutin, Xiaobin Yin, Paul Spurgeon, Steven Delwart

To cite this version:

Jean-Luc Vergely, Philippe Waldteufel, Jacqueline Boutin, Xiaobin Yin, Paul Spurgeon, et al.. New total electron content retrieval improves SMOS sea surface salinity. Journal of Geophysical Research. Oceans, 2014, 119 (10), pp.7295-7307. 10.1002/2014JC010150 . hal-01072107

HAL Id: hal-01072107
https://hal.science/hal-01072107v1

AGU PUBLICATIONS

JGR

Journal of Geophysical Research: Oceans

RESEARCH ARTICLE

10.1002/2014JC010150

Special Section:

Early scientific results from the salinity measuring satellites Aquarius/SAC-D and SMOS

Key Points:

- Total electron content is estimated from third Stokes parameter SMOS data
- Using third Stokes information improves the quality of salinity retrievals

Correspondence to:

P. Waldteufel,
philippe.waldteufel@latmos.ipsl.fr

Citation:

Vergely, J.-L., P. Waldteufel, J. Boutin, X. Yin, P. Spurgeon, and S. Delwart (2014), New total electron content retrieval improves SMOS sea surface salinity, *J. Geophys. Res. Oceans*, *119*, 7295–7307, doi:10.1002/2014JC010150.

Received 19 MAY 2014
Accepted 1 OCT 2014
Accepted article online 6 OCT 2014
Published online 29 OCT 2014

New total electron content retrieval improves SMOS sea surface salinity

Jean-Luc Vergely[1], **Philippe Waldteufel**[2], **Jacqueline Boutin**[3], **Xiaobin Yin**[3], **Paul Spurgeon**[4], **and Steven Delwart**[5]

[1]ACRI-ST, Sophia Antipolis, France, [2]LATMOS, Guyancourt, France, [3]LOCEAN, UPMC, Paris, France, [4]ARGANS, Plymouth, UK, [5]ESA/ESRIN, Roma, Italy

Abstract The European Space Agency (ESA)-led SMOS (Soil Moisture and Ocean Salinity) mission aims at monitoring both soil moisture (SM) and ocean surface salinity (OS) on a global scale. The SMOS instrument is a microwave interferometric radiometer, which provides visibilities, from which brightness temperatures (TB) maps are reconstructed in the spacecraft' antenna reference frame. In this study, we investigate how to improve the retrieval of salinity thanks to a better knowledge of the ionospheric total electron content (TEC). We show how both the SMOS bias correction (the so-called Ocean Target Transformation, OTT) and the half orbit TEC profile can be obtained from SMOS third Stokes parameter A3 using a location on the SMOS field of view (FOV) where the sensitivity of TB to TEC is highest. The resulting TEC global maps compare favorably with those built from the International Global navigation satellite system Service observations. TEC values obtained from A3 are next used to optimize the OTT estimation for every polarization, and proved to provide more stable values. Finally, improvements achieved in the salinity retrieved from SMOS data are reported.

1. Introduction

Since it was launched in November 2009, the European Space Agency (ESA)-led SMOS (Soil Moisture and Ocean Salinity) space mission [*Mecklenburg et al.*, 2012] has been delivering data aimed at monitoring both soil moisture (SM) and ocean surface salinity (OS) on a global scale. The measurement is based on the dependence of surface emissivity—and thus radiometric brightness temperatures (TB)—on SM and OS. The L-band was found an optimal compromise for both quantities, notwithstanding the poor dTB/d(OS) sensitivity.

The interferometric radiometer on board SMOS provides a sequence of snapshots, i.e., 2-D maps of TB for every polarization, from which, for each location on surface, a set of TB values for a range of incidence angles is reorganized and obtained [*Kerr et al.*, 2010].

Then the retrieval method applied over ocean essentially finds the salinity which minimizes a cost function over this set, using a direct radiative model and introducing both auxiliary data and a priori constraints derived from available auxiliary information [*Zine et al.*, 2008].

The SMOS interferometric data (visibilities) allow to reconstruct TB maps in the reference frame associated to the spacecraft antenna. Actually, the corresponding electric fields differ from the upwelling radiation through a rotation, the angle of which depends on geometrical factors and has come to be referred to as the "Claassen" angle [*Claassen and Fung*, 1974; *Waldteufel and Caudal*, 2002]. To this deterministic transformation is added the Faraday rotation, which is induced by the total electron content encountered along the Spacecraft-to-Earth line of sight throughout the Earth ionosphere.

Although many results have been obtained which demonstrate the physical meaning of salinity and soil moisture values obtained from SMOS retrievals [*Reul et al.*, 2013; *Kerr et al.*, 2012], the processing still suffers from some weaknesses.

A residual, not fully explained offset, has been identified with respect to the forward simulated ocean scene brightness model. While this offset appears to be stable over several days, it depends on the location in the SMOS field of view (FOV). It is currently corrected through the so-called Ocean Target Transformation (OTT); the OTT is specific of each location as defined by director cosine coordinates (ξ, η) in the antenna reference frame [*Yin et al.*, 2013a]. The OTT is empirically formulated as an additive correction and estimated, using a radiative model, as an average over an ocean area free from land contamination and radio frequency interferences [*Yin et al.*, 2012].

In addition, discrepancies between the reconstructed third Stokes parameter A3 and the behavior expected from radiative models as a function of the incidence angle are still under investigation.

Results reported here show how it appears however possible to retrieve the nadir total electron content (TEC) from A3, taking advantage of the particular geometry of the FOV, and to make use of it to obtain thereafter an improved estimate of the OTT bias correction. Only the case of ocean surfaces, which is the most critical in terms of measurement errors, is considered.

Section 2 deals with sensitivity of the TB to TEC and shows it to be highest for A3 and for a specific (ξ, η) location on the SMOS FOV. Further analyses show how, for such a location, both the OTT correction for A3 and the half orbit TEC profile can be obtained. Finally, a comparison is presented between TEC global data obtained from A3 and TEC maps built from the International Global navigation satellite system Service (IGS) observations.

Section 3 proposes a way to obtain the TEC over the whole FOV; it then becomes possible to select optimal TEC values for each incidence angle. At the same time, new TEC values are introduced in the OTT estimation for TB components TX and TY and proved to provide more stable results for the OTT bias correction. Finally, positive indications are presented as to the improvements achieved in the salinity retrieved from SMOS.

The conclusion summarizes the results obtained so far, points out some open questions and proposes further developments.

2. Estimating TEC From Stokes 3 SMOS Measurements

This section first recalls how the Faraday rotation depends on the total ionospheric content; it then presents an analysis of TB sensitivities to TEC. On this basis, a method is proposed to obtain meridian TEC profiles from the Stokes 3 component. Finally, resulting TEC profiles are compared to TEC maps built using GPS observations.

2.1. TEC for Processing SMOS Data

The Faraday rotation angle ω_F depends on TEC and the geomagnetic angles. It can be written [*Le Vine and Abraham*, 2000]:

$$\omega_F = 6950\ \mathrm{TEC}/\cos(\theta)\mathbf{P}.\mathbf{B} \tag{1}$$

with

ω_F expressed in degrees;

TEC the vertical total electron content below the spacecraft expressed in TEC units: TECu (1 TECu = 10^{16} electrons/m^2);

θ the incidence angle at ground level;

P the unit vector along the line of sight from spacecraft to ground; and

B the magnetic field vector for a representative average altitude (typically 400 km).

In the present SMOS operational processing chain, the Faraday angle is considered as a fully external auxiliary parameter and supplied as a level 1 output according to the SMOS Algorithm Theoretical Baseline Document for Level 1 [*Gutierrez*, 2006].

The geomagnetic vector B is computed using the International Geomagnetic Reference Field (IGRF) model [*Barton*, 1997]; TEC values are obtained using the IGS products [*Crapolicchio*, 2008].

2.2. TB Sensitivity to TEC Over the Field of View

We now consider the field of view (FOV) of SMOS, in the antenna reference frame. The FOV limits, as depicted in Figure 1, are mainly imposed by taking into account aliasing. Lines of constant incidence angles (Figure 1d) are circles centered on the nadir location.

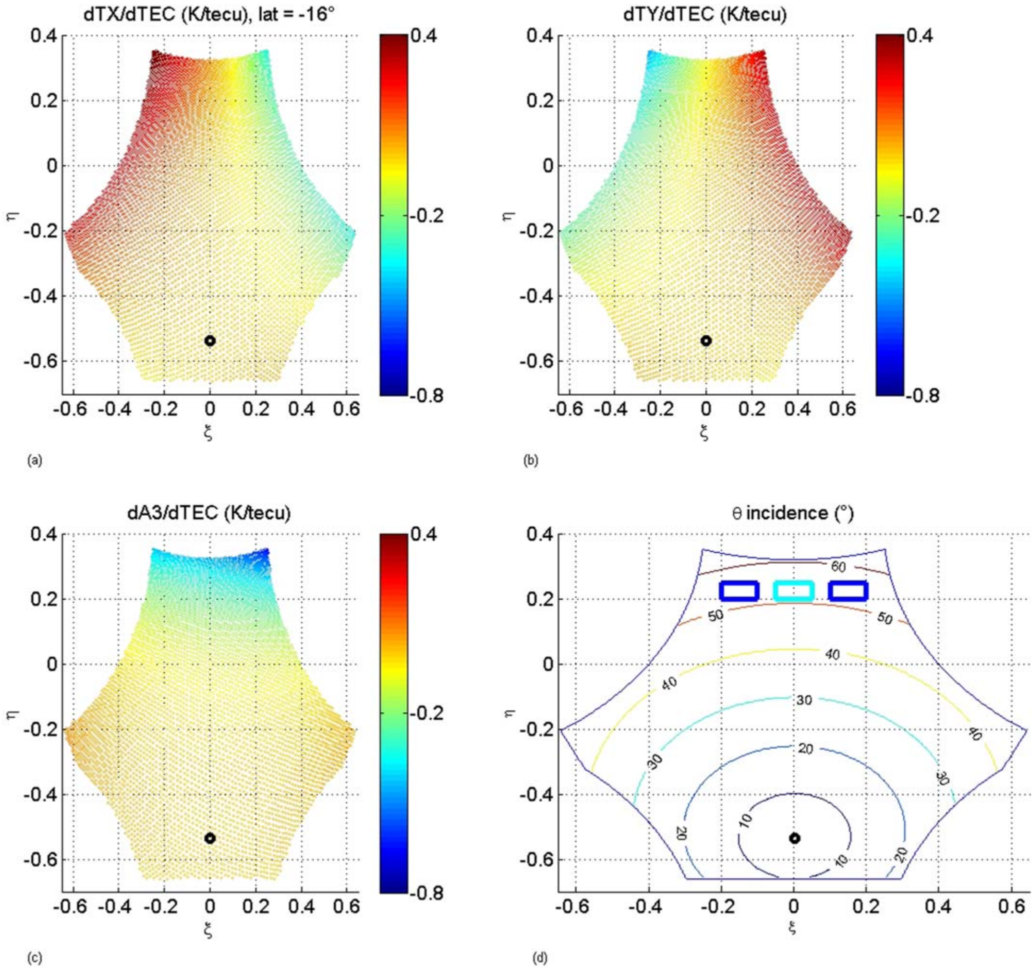

Figure 1. (a–c) Sensitivity of brightness temperatures TX, TY, and A3 in the antenna frame to TEC over the FOV for flat ocean, T4 = 0, descending orbits. (d) Isocontours for constant incidence angle. The area selected for estimating TEC is also indicated (light blue rectangle); dark blue rectangles delineate regions where sensitivities to TEC are later computed and shown in Figure 3.

The upwelling radiation is defined by brightness temperatures for horizontal and vertical polarizations TH and TV, complemented by the third and fourth Stokes parameters, T3 and T4 at surface level. In the SMOS antenna reference frame, the radiation is defined by brightness temperatures along perpendicular axes TX and TY and the third and fourth Stokes parameters noted A3 and A4 at antenna level.

The brightness temperatures at antenna level are obtained from the surface level TB using the following transformation matrix [*Waldteufel and Caudal*, 2002]:

$$\begin{bmatrix} TX \\ TY \\ A3 \\ A4 \end{bmatrix} = \begin{bmatrix} \cos^2(a) & \sin^2(a) & -\cos(a)\sin(a) & 0 \\ \sin^2(a) & \cos^2(a) & \cos(a)\sin(a) & 0 \\ \sin(2a) & -\sin(2a) & \cos(2a) & 0 \\ 0 & 0 & 0 & 1 \end{bmatrix} \begin{bmatrix} TH \\ TV \\ T3 \\ T4 \end{bmatrix} \tag{2}$$

With

$$a=\psi+\omega_F \tag{3}$$

where ψ is the "Claassen" angle and ω_F the Faraday rotation angle.

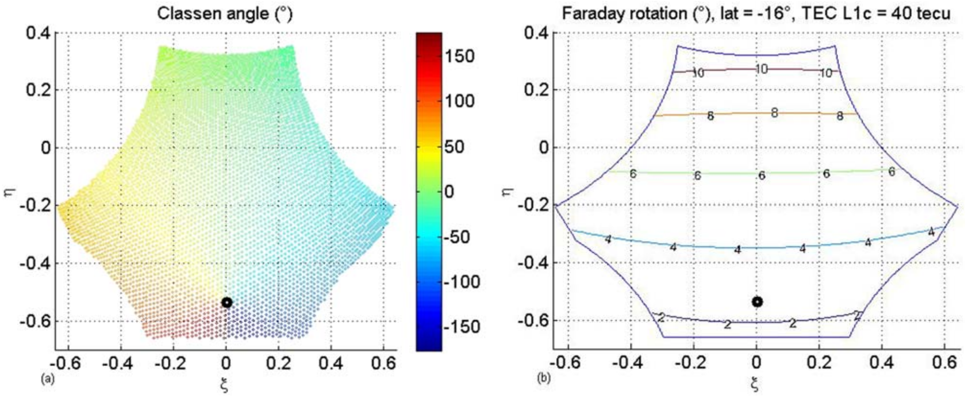

Figure 2. a. Map of the Claassen angle ψ over the SMOS FOV. b. Faraday angle computed for a descending orbit, at a 16°S latitude, with a uniform TEC = 40 TECu.

Assuming the upwelling Stokes T4 is negligible, the matrix becomes:

$$\begin{bmatrix} TX \\ TY \\ A3 \\ A4 \end{bmatrix} = \begin{bmatrix} \cos^2(a).TH+\sin^2(a).TV-\cos(a)\sin(a).T3 \\ \sin^2(a).TH+\cos^2(a).TV+\cos(a)\sin(a).T3 \\ \sin(2a).TH-\sin(2a).TV+\cos(2a).T3 \\ 0 \end{bmatrix} \tag{4}$$

The sensitivities of brightness temperatures to the TEC for TX, TY, and A3 are shown in Figures 1a–1c. The Claassen angle and representative Faraday angles are shown in Figures 2a and 2b.

We next write the derivatives of brightness temperatures with respect to TEC. From equations (3) and (4), we obtain:

$$\begin{bmatrix} dTX/dTEC \\ dTY/dTEC \\ dA3/dTEC \\ dA4/dTEC \end{bmatrix} \approx \begin{bmatrix} -2\cos(a).\sin(a).(TH-TV)-\cos(2a).T3 \\ 2\cos(a).\sin(a).(TH-TV)+\cos(2a).T3 \\ 2\cos(2a).(TH-TV)-2\sin(2a).T3 \\ 0 \end{bmatrix} d\omega_F/dTEC \tag{5}$$

Keeping in mind that the T3 contributions are comparatively very small, the matrix factor developed in equation (5) explains several features depicted in Figure 1:

1. The sensitivity of TX and TY to TEC is weak in the area of the FOV where the incidence angles are small, since TH and TV are then close to each other.
2. More generally, areas with high incidence angles, as indicated in Figure 1d, correspond to better sensitivities since the (TH-TV) differences are larger there.
3. Furthermore, when the *a* angle approaches either 0° (close to the track) or 90°, then cos(*a*).sin(*a*) becomes close to 0: therefore, the sensitivity of TX and TY to TEC will be weak close to the track, whereas for A3 the sensitivity is highly dependent on the $d\boldsymbol{\omega}_\mathbf{F}$/dTEC factor.
4. Conversely, when the *a* angle approaches 45°, the sensitivity to TEC is maximum for TX and TY, the reverse being true for A3.

Overall, the region of the FOV with the highest sensitivity to TEC is found for Stokes 3, in the area where the incidence angles are close to 60°.

Based on the above analysis, the best area in the FOV for computing TEC from A3 appears to be circa [$\boldsymbol{\xi} = 0$, $\boldsymbol{\eta} = 0.2$], as illustrated in Figure 1d.

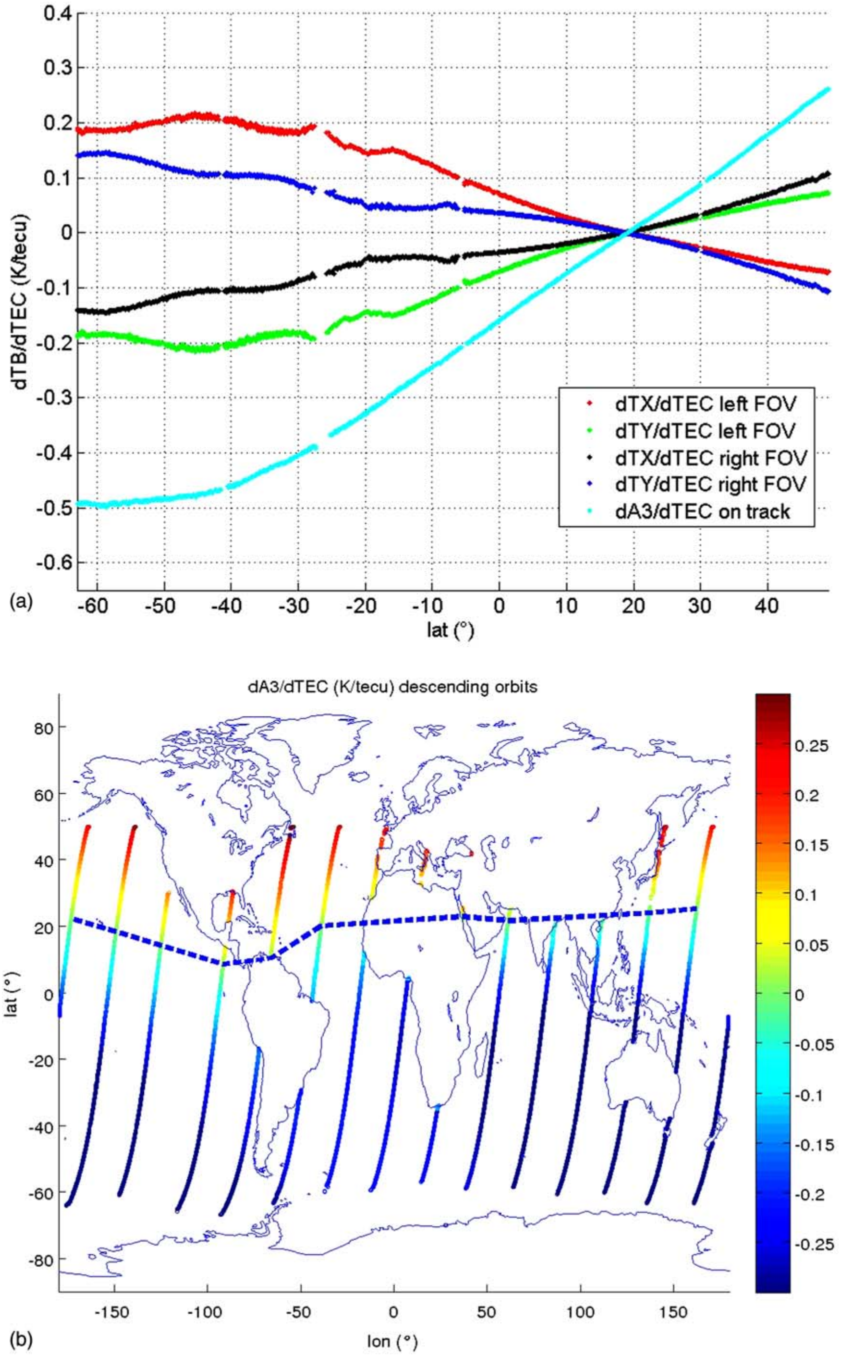

Figure 3. (a) Sensitivity of brightness temperatures to TEC for several FOV areas (shown in Figure 1d) along a SMOS descending half orbit as a function of the spacecraft latitude. (b) Sensitivity of A3 to TEC over ocean areas for the light blue FOV rectangle shown in Figure 1d (descending orbits). The dotted line shows the latitude where dA3/dTEC = 0.

It must be noted also that the sensitivity to TEC will decrease to zero when the angle between the line of sight and magnetic field vector **B** is close to 90°.

In Figure 3a, the sensitivity of measured brightness temperatures to TEC, in the rectangular areas identified in Figure 1d, is depicted as a function of the spacecraft latitude for descending orbits. It is seen that the sensitivity becomes close to zero for latitudes around 15° north; in this geographic area, the line of sight is indeed nearly orthogonal to the magnetic field vector.

Figure 3b shows how the above mentioned "TEC blind" latitude band depends little on longitude.

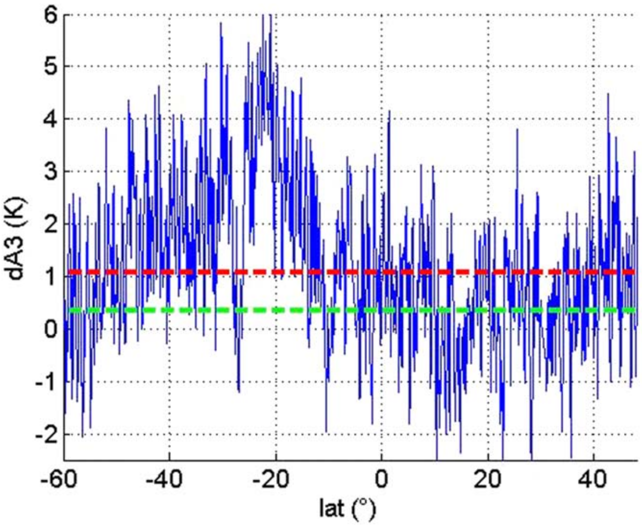

Figure 4. A3 increment (the right-hand side of equation (6)) along a descending SMOS half orbit. The green and red dotted lines stand, respectively, for the OTT obtained when selecting the value for the 15° latitude and when averaging over the whole half orbit.

When investigating issues associated to TEC, it is best to deal with large values, in order to maximize the TEC signals with respect to radiometric noise. Hence, descending orbits are selected, inasmuch as they occur close to 6 P.M., near the local time of ionospheric diurnal maximum.

2.3. Recovering a TEC Value Over a Half Orbit Track

We begin with the first guess TEC_{L1} available from SMOS level 1. Using a radiative model [*Zine et al.*, 2008], we compute a value $A3_M(TEC_{L1})$ for A3. An expression for an improved TEC estimate TEC_{A3} may then be written for every abscissa along the orbit, introducing the difference between observed and model A3 values, and including the OTT correction:

$$TEC_{A3} \approx TEC_{L1} + \frac{dTEC}{dA3}\left(A3 - A3_M(TEC_{L1}) - OTT\right) \qquad (6)$$

where both the A3 polar component and the OTT correction stand for the values at the $[\xi = 0, \eta = 0.2]$ location in the FOV.

When applying equation (6) everywhere along the half orbit, the OTT value does not change; however, this value remains now to be determined. To this end, we consider the latitude zone around 15°N, as shown in Figure 2, where the TB sensitivity to TEC dA3/dTEC is vanishing; there equation (6) can be simplified as follows:

$$OTT = A3 - A3_M(TEC_{L1}) \qquad (7)$$

In this latitude zone, since the Faraday rotation vanishes, there is no impact of the TEC on any brightness temperature. Equation (7) supplies the requested OTT value to be inserted in equation (6). Knowing that the OTT is found to be stable over a couple of weeks, a half orbit with adequate latitude coverage over ocean for this purpose can easily be found.

Figure 4 plots $A3–A3_M(TEC_{L1})$ along a descending SMOS half orbit. The red dotted line shows which OTT correction value would result when averaging this increment over the whole half orbit. The green line, on the other hand, shows the OTT value estimated from A3 measured around a 15°N latitude. Such TB differences may reach up to 1 K, which is quite significant when one is concerned with salinity retrieval.

Figure 5 shows examples of both TEC_{L1} and TEC_{A3} profiles with latitude.

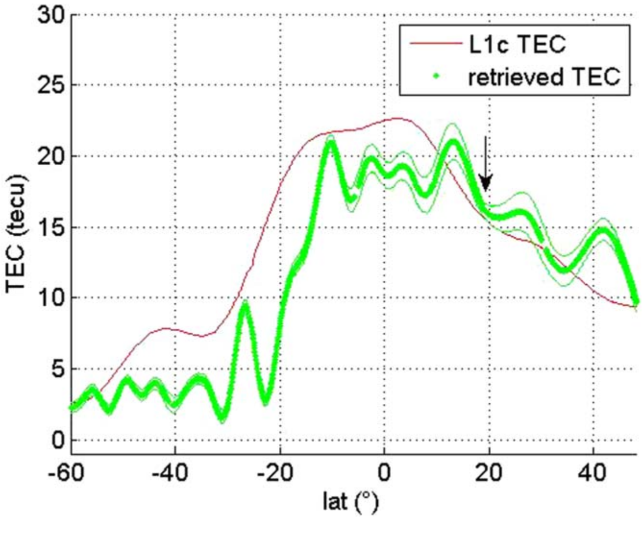

Figure 5. TEC_{A3} (green line) from equation (6) and TEC_{L1} (red line) from L1 SMOS processing.

When implementing the above method, TEC_{A3} and OTT are estimated simultaneously over the A3 profile, using a standard Bayesian least squares approach [*Tarantola*, 1987],

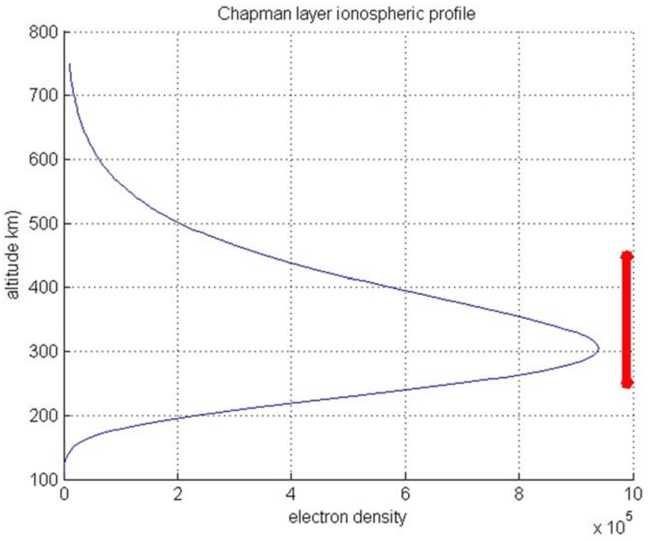

Figure 6. Representative ionospheric F layer using a Chapman photoionization model with a constant 60 km scale height. The red thick line shows the mean altitude ±1 standard deviation.

with TEC_{L1} chosen as the a priori value. The TEC_{A3} values retrieved along track are smoothed using a Gaussian filter with a 300 km width, in order to reduce noise. Around the "TEC-blind" area, the algorithm tends to retrieve the a priori value. Small fluctuations present on the TEC_{A3} curve are understood to be mostly due to the remaining noise; their amplitude is of the order of 3 TECu, depending on the latitude.

While the latitude indicated in abscissa in Figure 5 corresponds to the location where the Spacecraft-to-Earth line of sight intersects the surface, it remains to determine which latitude ought to be assigned to the TEC_{A3} values. The most adequate location (hence latitude) is the one where the bulk of ionospheric contributions originates from, noting (from Figure 1d) that the incidence angle is about 50°. While the ionosphere cannot be assimilated to a very thin horizontal layer, a simple Chapman layer model [*Rishbeth and Garriott*, 1969] yields for the ionospheric F layer a mean altitude around 350 km (for a 20° sun incidence angle) and a standard deviation of the profile along the vertical of about 90 km (Figure 6). For a 60° incidence angle, the horizontal spread of the contributing layer then extends over ±150 km around the mean layer altitude. This allows defining the relevant latitude for each TEC estimate with an accuracy which is, at any rate, substantially better than the latitudinal extent (circa 1200 km) of the SMOS geographical FOV.

As a consequence, while TEC values shown in Figure 5 are plotted for latitudes where the line of sight intersects the surface, the TEC_{A3} profile should be assigned to latitudes shifted by about 5° northward.

2.4. TEC Comparisons

The Figure 7a shows a map of TEC obtained from combined GPS files (ftp://cddis.gsfc.nasa.gov/gps/products/ionex/) for 3 h Universal Time (UT). These files have actually been combined from contributions by several IGS Ionosphere Associate Analysis Centers [*Hernández-Pajares*, 2003]. The superimposed SMOS orbit shows that the descending half orbit occurs close to the daily maximum of the TEC in the middle afternoon, while the ascending one is close to the minimum.

The Figure 7b next shows a map of the same combined GPS files for the SMOS descending half orbit over 427 descending orbits in May 2011, that is for a constant local time (LT) around 6 P.M.; Figure 7c presents a similar 6 P.M. LT map for the TEC extracted using the A3 data.

While the bimodal maximum along a meridian was hardly visible on the UT map in Figure 7a, it now appears as a major feature for both GPS TEC and TEC_{A3} constant LT maps. This feature is mostly apparent in the Pacific Ocean zones. It is more marked for TEC_{A3} for which the spatial resolution induced by the smoothing function is about 300 km, while for the GPS data it is at best 550 km along a meridian, due to the step of the interpolation grid.

We are observing here the well-known equatorial anomaly associated to the "equatorial fountain" mechanism [e.g., *Rishbeth and Garriott*, 1969]: the combined effect of plasma diffusion along lines of the Earth's magnetic field and motion across the field lines generated by an assumed distribution of eastward electric field induces a deep ionospheric "trough" centered on the magnetic equator.

At the global scale, an asymmetry is noted between the North and South hemispheres, for both TEC maps in Figures 7b and 7c, with larger values in the North hemisphere. This might be expected at this time of

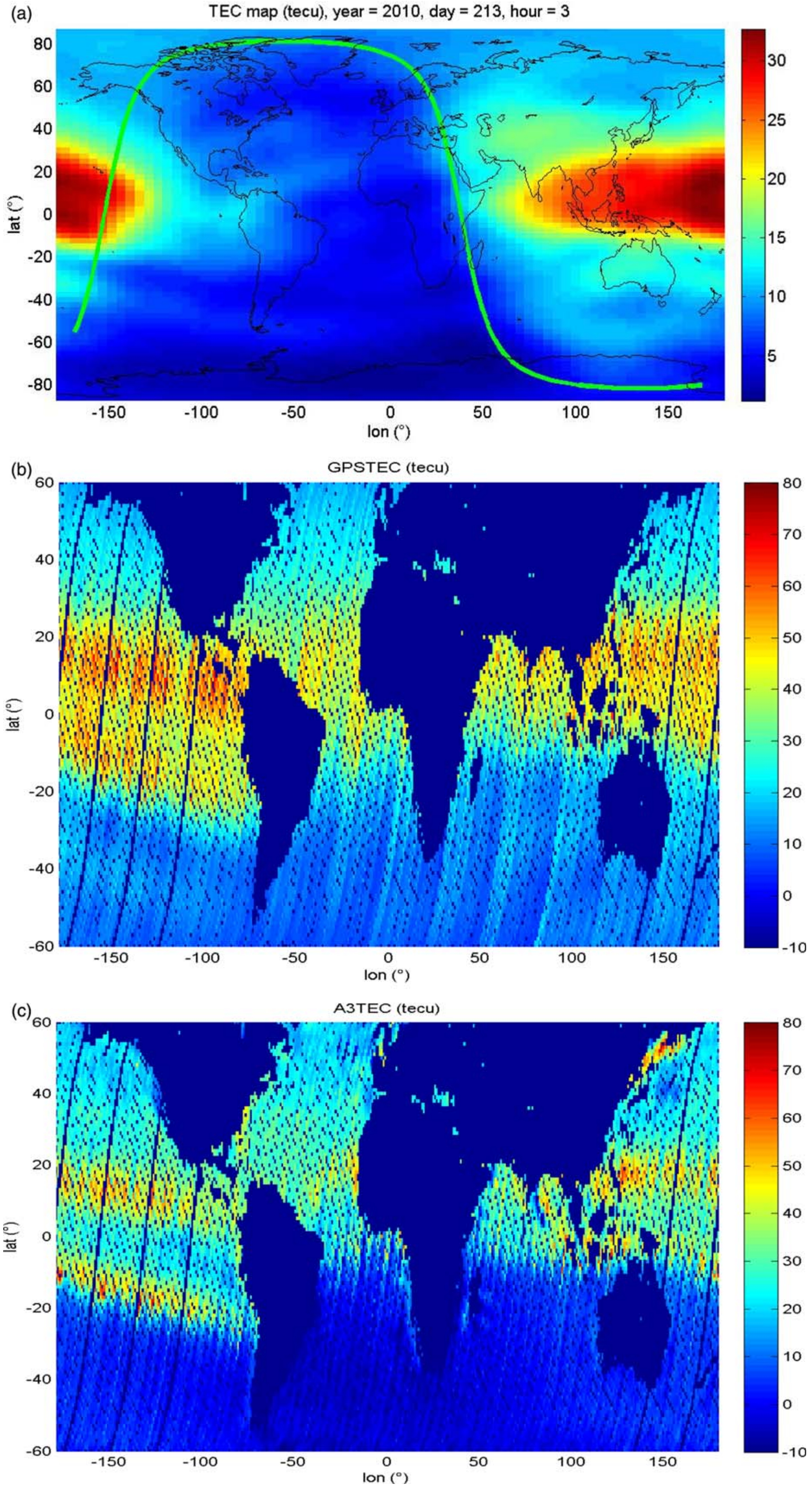

Figure 7. (a) Example of a global TEC map built from combined ionosphere map exchange (IONEX) GPS products. (b) Local time 18 h map for TEC derived from GPS data. (c) Local time 18 h map for TEC derived from SMOS Stokes 3.

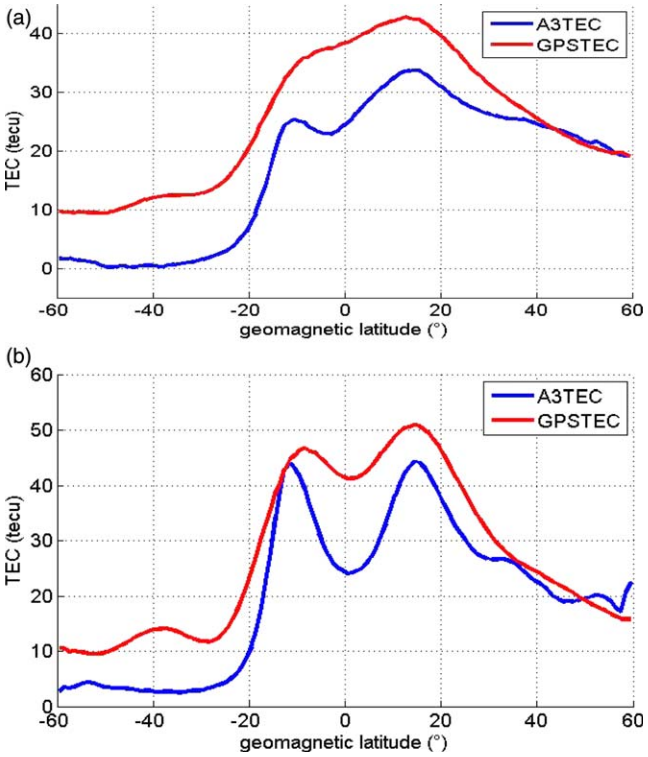

Figure 8. (a) Meridian profiles (in geomagnetic coordinates) for GPS TEC and TEC_{A3}, averaged over the whole globe. (b) Meridian profiles (in geomagnetic coordinates) for GPS TEC and TEC_{A3}, averaged over longitudes limited to the Pacific Ocean.

year. However, the asymmetry is more marked for TEC_{A3}, because values for high southern latitudes seem abnormally low.

The Figures 8a and 8b show the meridian GPS TEC and TEC_{A3} profiles, averaged first over all longitudes (Figure 8a), then on longitudes restricted to the Pacific Ocean (Figure 8b). These two figures are presented in geomagnetic coordinates, which supply a natural reference frame when considering physical parameters such as ionospheric TEC.

While in Figure 8a the equatorial anomaly has been partially smeared by averaging over all longitudes, in Figure 8b the bimodality of TEC is clearly seen. Same as for Figures 7b and 7c, the anomaly appears with better clarity on the TEC_{A3} profile.

Other large-scale discrepancies are noted. For high southern latitudes, TEC_{A3} decreases until it practically vanishes, while the GPS TEC remains of the order of 5 TECu; for high northern latitudes, conversely, TEC_{A3} tends to exceed somewhat the GPS TEC.

3. TEC and OTT Correction for Salinity Retrieval

This section first argues that TEC track profiles computed in section 2 can be used for obtaining the Faraday rotation at every location of interest on the FOV. This result is next used for computing the OTT correction for every polarization; this is shown to improve the stability of resulting OTT maps. Finally, the impact of improved OTT corrections and estimates of the Faraday rotation on the retrieved salinities is demonstrated.

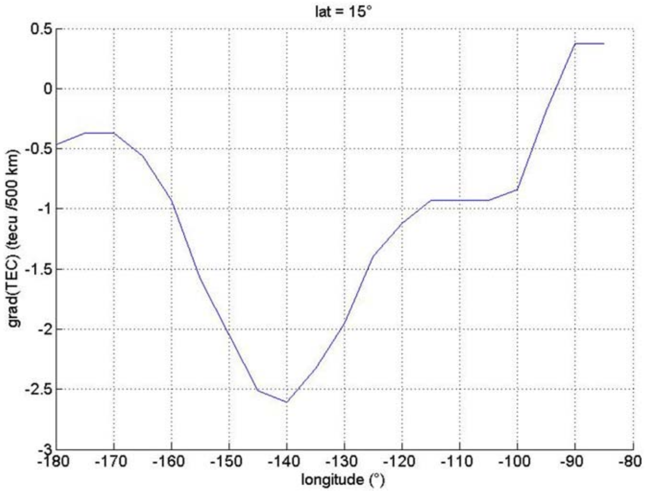

Figure 9. Variation of TEC (taken from the global map shown in Figure 7a) over 500 km along the parallel circle for the latitude (15°) where the highest TEC values are observed.

3.1. Extended Approximation of the TEC Across the FOV

So far, the TEC_{A3} values have been retrieved along the track. The question arises to which extent these values can be used further across the SMOS FOV.

Figure 9 shows the gradient of TEC along a parallel for the latitude (here 15°N) where the highest TEC values are observed in Figure 7a: this gradient reaches at most 2.5 TECu over a 500 km range.

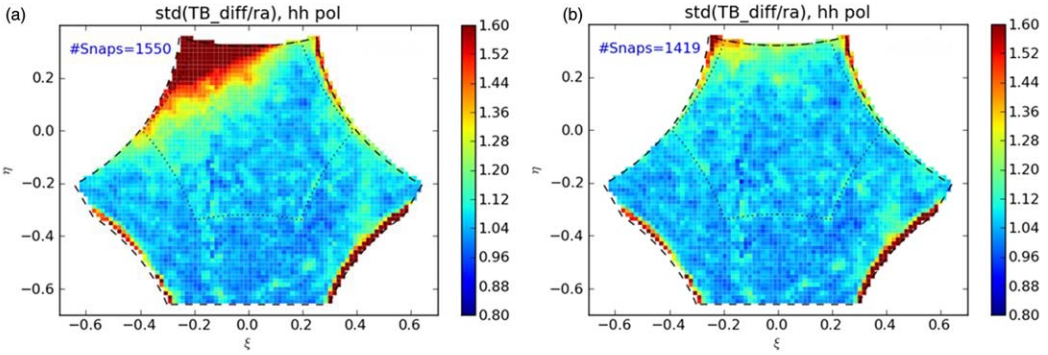

Figure 10. Standard deviation of the OTT_{TX}, normalized to radiometric accuracy, using (left) L1 and (right) A3 TEC estimates. The snapshot samples were taken in the South East Pacific Ocean.

The width of the swath across the FOV currently used for OS and wind retrieval is $\pm\approx 300$ km [*Yin et al*., 2013b]. Since the SMOS polar orbit is quasicircular at a 758 km altitude, to be compared to circa 350 km for the average level of the ionospheric layer, this results in a width narrowed down to $\pm\approx 150$ km for TEC locations; within these limits, according to Figure 9, TEC variations should then be at most of the order of 1 TECu. For the purpose of the present analysis, and in view of uncertainties reported in section 2.1, such across track variations of the TEC will be neglected.

3.2. From New TEC Estimates to Improved OTT Corrections

Before using the brightness temperatures TX and TY as inputs for salinity retrieval, the TB biases within the FOV have to be removed using the OTT correction. This correction is estimated as the average over a selected half orbit of the difference between the reconstructed TB and the TB computed using a radiative model over a stable oceanic zone as free as possible of artifacts.

It is now possible to take advantage of the new estimation TEC_{A3} when computing these model values for TX and TY:

$$OTT_{TX} = < TX - TX_M(TEC_{A3}) > \tag{8}$$

where the "$< >$" notation refers to the averaging procedure over a stable oceanic zone as mentioned above, and equation (8) is written for every (ξ, η) location on the FOV. Finally, the TX are corrected using OTT_{TX}; the same method is applied for TY.

Figure 10 presents a map of the standard deviation of the OTT_{TX} both before and after the TEC_{A3} values have been used as indicated in equation (8). While effects are hardly apparent in areas where the sensitivity to TEC is very weak, the OTT standard deviation is strongly reduced in the front FOV area. The overall impact of this improved stability is found quite significant in terms of retrieved salinity.

This result demonstrates that much of fluctuations in the OTT correction so far were in fact due to a poor estimation of the TEC. It confirms the stability over a few weeks of the OTT correction after the TEC has been properly accounted for; moreover, this stability with time may help to better understand the OTT correction in order to be able to reduce its magnitude in the future.

3.3. Impact on Salinity Retrievals

To investigate the impact of using the improved TEC estimates, we have compared both salinity standard retrievals and salinity retrievals using the TEC_{A3} values to ARGO interpolated maps. The TB inputs in the retrievals are taken from the reprocessed SMOS level 1C version 505 for May 2011.The quality of the retrieved SMOS salinities was evaluated by comparing them with surface ARGO interpolated salinity maps as described in *Hernandez et al*. [2014], filtering out SMOS pixels less than 700 km away from any coast in order to avoid contaminations by land surfaces. When salinity was retrieved by means of the standard level 2 ocean salinity processor v550, using TEC_{L1} both for computing the OTT and as a prior in the iterative retrieval, the retrieved salinity exhibited positive biases at high latitudes (Figure 11, top). Such biases are significantly reduced when the new TEC retrieval is implemented in processor v611 (Figure 11, bottom). Additional tests (not shown) conducted using TEC_{A3} either only in the OTT computation,

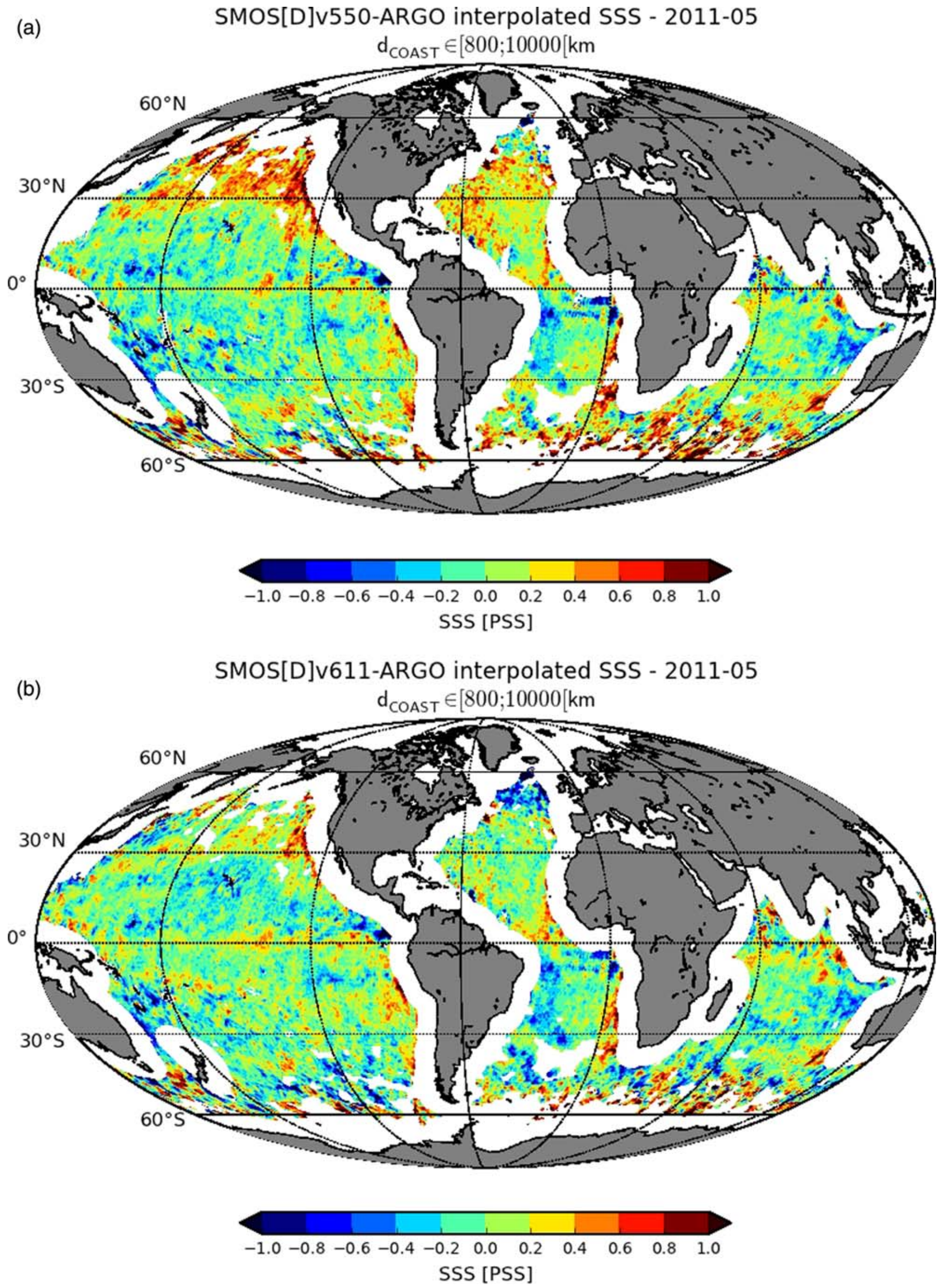

Figure 11. SMOS OS minus ARGO OS interpolated maps, May 2011, descending orbits. (top) SMOS OS retrieved with default L2 processor v550. (bottom) SMOS OS retrieved with the TEC_{A3} as described in this paper. Note the improvement in the latitudinal bias.

or only as an improved auxiliary TEC data set when retrieving OS, did not show such improvements, confirming the need to include TEC_{A3} in both computations. It must however be stressed that the main improvement comes from the contribution of TEC_{A3} when computing the OTT. This explains why, in some regions, retrieved OS values exhibit significant differences although the local TEC values undergo little change.

Biases and standard deviations (std) of SMOS-ARGO salinity differences are reported in Table 1. Both mean biases and std are reduced when the TEC estimated from A3 is introduced, whatever the region considered. In addition, with the TEC_{A3} algorithm, std obtained during descending orbits become closer to those estimated for ascending orbits, within 10%, or even almost identical in tropical regions.

Table 1. SMOS OS From Descending Orbits Versus ARGO Interpolated OS Maps for May 2011

L2 V550 Processing: TEC_{L1c} Used Both as Prior and in OTT Computation			L2 V611 Processing: TEC_{A3} Used Both as Prior and in OTT Computation		
Zone	Mean	Std	Zone	Mean	Std
60°S 60°N	0.11	0.39	60°S 60°N	0.02	0.36
45°S 45°N	0.05	0.32	45°S 45°N	0.01	0.29
30°S 30°N	−0.01	0.29	30°S 30°N	0.02	0.27

4. Summary and Conclusions

Our sensitivity study has indicated that the A3 Stokes component (Stokes 3 in the antenna reference frame) exhibits the highest sensitivity to TEC in the front part of the SMOS Field of View. We have shown how it is possible to compute an improved OTT correction which yields a bias-free estimation of TEC over the whole half orbit track. While the computations have been performed with SMOS level 1 data v505, the A3 OTT is expected to be much reduced with the updated L1 processor to be released in the near future, thanks to recent improvements in the image reconstruction algorithm. Hence, one could expect and hope that the magnitude of the OTT correction will decrease with future releases of the SMOS L1 data. For example, it is expected that the contamination of A3 by cross-polar contributions leaked from TX and TY [*Wu et al*., 2013] will be explicitly taken into account by future versions of the processing chain, rather than being compensated by a part of the empirical OTT correction.

We have compared SMOS-derived TEC to TEC maps based on GPS measurements. Overall satisfactory agreement is found; the well-known equatorial anomaly is present and emphasized in the SMOS-derived TEC, owing most probably to the better spatial resolution.

The new TEC estimation is used in turn to improve the pixel-dependent OTT correction for every polarization component and location on FOV; the resulting correction clearly shows better stability. Finally, a better agreement is obtained between retrieved salinities and ground truth data.

The TEC_{A3} estimation should not however be considered as fully validated at this stage. Specifically, while the enhanced representation of the equatorial anomaly is encouraging, we have to validate it against other TEC data with better spatial resolution than the maps built from GPS measurements. In this respect altimetry data are obvious candidates, with better coverage over ocean surfaces.

In the same spirit, it is necessary to investigate the discrepancies for high latitudes, especially on the southern hemisphere where TEC_{A3} values are found close to zero. Concerning the forward radiative model, the (TH-TV) differences might be incorrect due to an inadequacy of the roughness model in these high wind regions, and/or of the dielectric model for cold waters known to prevail there; similarly, in such conditions, the upwelling Stokes 3 component might be larger than predicted. In depth investigations coordinated with the Aquarius team [*Lagerloef et al*., 2008] are called for. Interestingly, a test performed on Aquarius data during the same season (although for a different year) indicates at first order a similar meridian distribution of TEC [*Dinnat et al*., 2014].

In the present paper, we have considered only the FOV region with the highest sensitivity to TEC. The technique might be extended elsewhere on the FOV, giving access to TEC information obtained for a variety of incidence angles. This deserves attention because it should allow us to optimize the altitude selected for the equivalent ionospheric "slab" layer, and ultimately optimize the geographical localization for estimated TEC values.

Finally, it is expected that the TEC itself obtained from SMOS may deserve to be investigated more in detail. For example, it is well known that magnetic storms induce strong disturbances in the ionospheric F2 layer [*Rishbeth and Garriott*, 1969] and thus the TEC behavior. Such phenomena should not be ignored when the TEC is introduced in the frame of corrections (which is the case, e.g., for SMOS and surface salinity); alternatively, TEC profiles obtained from SMOS might bring useful additional information on the effect of magnetic storms.

We have focused the present study on SMOS data collected over the oceans. True to say, the sensitivity conditions are such that the impact of ionospheric corrections is weaker over the continents. However, the improvements discussed above, when achieved over oceans, will also be of benefit over the continents when estimating soil moisture and other surface parameters.

Acknowledgments
This work was supported in part by ESRIN/contracts 1-6704/11/I-AM (SMOS+ polarimetry) and 3-13003/10/I-OL (SMOS phase E) and by CNES/TOSCA SMOS-OCEAN contract. We are grateful to Elvira Astafyeva for helpful discussions, to Nicolas Martin for performing SMOS-ARGO collocations, and to Emmanuel Dinnat for carrying out an encouraging test on Aquarius data. SMOS Level 1 and 2 data are available from ESA upon request submitted to the EO help desk eohelp@esa.int.

References

Barton, C. E. (1997), International geomagnetic reference field: The seventh generation, *J. Geomagn. Geoelectr.*, *49*, 123–148.

Claassen, J. P., and A. K. Fung (1974), The recovery of polarized apparent temperature distributions of flat scenes from antenna temperature measurements, *IEEE Trans. Antennas Propag.*, *AP-22*, 433–442.

Crapolicchio, R. (2008), VTEC usage for the SMOS Level 1 operational processor (L1-OP), *ESA Tech. Note XSMS-GSEG-EOPG-TN-06–0019*, ESA/ESRIN, 00044 Frascati, Italy.

Dinnat, E., et al. (2014), Comparison of SMOS and Aquarius Sea Surface Salinity and analysis of possible causes for the differences, paper presented at XXXIst URSI General Assembly and Scientific Symposium, Beijing, 16–23 Aug, NASA-GSFC, Greenbelt, Md.

Gutierrez, A. (2006), SMOS L1 processor Algorithm_Theoretical Baseline Definition, *DEIMOS Tech. Note SO-DS-DME-L1PP-0011*, 71 pp., DEIMOS Engenharia, Lisboa, Portugal.

Hernandez, O., J. Boutin, N. Kolodziejczyk, G. Reverdin, N. Martin, F. Gaillard, N. Reul, and J. L. Vergely (2014), SMOS salinity in the subtropical north Atlantic salinity maximum: 1. Comparison with Aquarius and in situ Salinity, *J. Geophys. Res.*, doi:10.1002/2013JC009610, in press.

Hernández-Pajares, M. (2003), Performances of IGS ionosphere TEC maps, 7th IGS Iono WG report, Technical University of Catalonia, Barcelona, Spain.

Kerr, Y. H., et al. (2010), The SMOS mission: New tool for monitoring key elements of the global water cycle, *Proc. IEEE*, *98*, 666–687.

Kerr, Y. H., et al. (2012), The SMOS soil moisture retrieval algorithm, *IEEE Trans. Geosci. Remote Sens.*, *50*(5), 1384–1403.

Lagerloef, G. S. E., et al. (2008), The Aquarius/SAC-D mission: Designed to meet the salinity remote sensing challenge, *Oceanography*, *21*(1), 69–81.

Le Vine, D. M., and S. Abraham (2000), Faraday rotation and passive microwave remote sensing of soil moisture from space, in *Microwave Radiometer Remote Sensing Earth's Surface Atmosphere*, edited by P. Pampaloni and S. Paloscia, pp. 89–96, VSP BV, Netherlands.

Mecklenburg, S., et al. (2012), ESA's soil moisture and ocean salinity mission: Mission performance and operations, *IEEE Trans. Geosci. Remote Sens.*, *50*(5), 1354–1366.

Reul, N., et al. (2013), Sea surface salinity observations from space with the SMOS satellite: A new means to monitor the marine branch of the water cycle, *Surv. Geophys.*, *35*(3), 681–722.

Rishbeth, H., and O. K. Garriott (1969), *Introduction to Ionospheric Physics*, 331 pp., Academic, N. Y.

Tarantola, A. (1987), *Inverse Problem Theory*, Elsevier, N. Y.

Waldteufel, P., and G. Caudal (2002), About off-axis radiometric polarimetric measurements, *IEEE Trans. Geosci. Remote Sens.*, *40*(6), 1435–1439.

Wu, L., F. Torres, I. Corbella, N. Duffo, I. Duran, M. Vall-llossera, A. Camps, D. Delwart, and M. Martin-Neira (2013), Radiometric performance of SMOS full polarimetric imaging, *Geosci. Remote Sens. Lett.*, *10*(6), 1454–1458.

Yin, X., J. Boutin, and P. Spurgeon (2012), First assessment of SMOS data over Open Ocean. Part I: Pacific Ocean, *IEEE Trans. Geosci. Remote Sens.*, *540*(5), 1648–1661.

Yin, X., J. Boutin, and P. Spurgeon (2013a), Biases between measured and simulated SMOS brightness temperature over ocean, *IEEE J. Selec. Top. Appl. Earth Obs. Remote Sens.*, *6*(3), 1341–1350, doi:10.1109/JSTARS.2013.2252602.

Yin, X., J. Boutin, N. Martin, P. Spurgeon, and J. Vergely (2013b), Errors in SMOS sea surface salinity and their dependency on a priori wind speed, *Remote Sens. Environ.*, *146*, 159–171, doi:10.1016/j.rse.2013.09.008.

Zine, S., J. Boutin, J. Font, N. Reul, P. Waldteufel, C. Gabarro, J. Tenerelli, F. Petitcolin, J. L. Vergely, and M. Talone (2008), Overview of the SMOS sea surface salinity prototype processor, *IEEE Trans. Geosci. Remote Sens.*, *46*(3), 621–645, doi:10.1109/TGRS.2008.915543.